ACS NANO

www.acsnano.org

ARTICLE

Dual-Step Chemical Treatment of Wafer-Scale Metal–Organic Chemical Vapor Deposition Grown Monolayer Molybdenum Disulfides

Juhwan Lim,[&] Anh Tuấn Hoàng,[&] Zhaojun Li, Tran Thi Ngoc Van, Jung-In Lee, Kihyun Lee, Nicolas Gauriot, Kyle Frohna, Takashi Taniguchi, Kenji Watanabe, Bonggeun Shong, Kwanpyo Kim, Samuel D. Stranks, Jong-Hyun Ahn,* Manish Chhowalla,* and Akshay Rao*

Cite This: *ACS Nano* 2025, 19, 34698–34707

Read Online

ACCESS | Metrics & More | Article Recommendations | Supporting Information

ABSTRACT: **Two-dimensional (2D) transition metal dichalcogenides (TMDs) possess distinct optical and electronic properties, making them promising candidates for optoelectronic applications. Recently, major advances in the wafer-scale growth of TMDs using the metal–organic chemical vapor deposition (MOCVD) have enabled their integration with standard electronics. However, such materials continue to suffer from defects and unwanted doping, which lower semiconductor performance, as exemplified by poor photoluminescence (PL) yield. Chemical treatment protocols have been shown to improve the PL yield in exfoliated and CVD-grown materials. Here, using PL, Raman microscopy, X-ray photoemission spectroscopy (XPS) and density functional theory (DFT) calculations, we develop chemical treatment protocols for wafer-scale MOCVD-grown monolayer MoS_2. The postgrowth treatment uses sulfide and TFSI-based ionic salts delivered via a solution process. We demonstrate a substantial PL enhancement ranging from 23 to 50 times, depending on the underlying MOCVD growth method of the MoS_2. We present design rules for tuning chemical treatment protocols, depending on the defect densities and doping levels, allowing for successful passivation and large PL enhancements across different growth conditions. Our results demonstrate the versatility of these chemical treatment protocols and their potential to improve PL in device-relevant wafer-scale MOCVD-grown monolayer TMDs.**

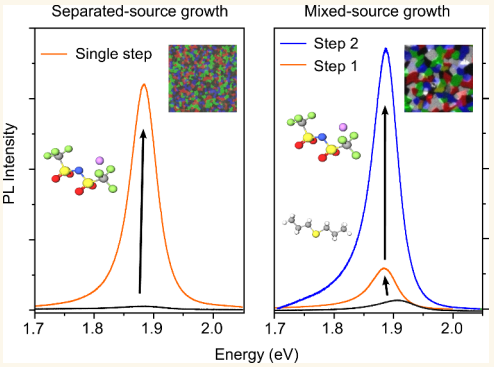

KEYWORDS: *metal–organic chemical vapor deposition, transition metal dichalcogenides, chemical treatment, defect passivation, photoluminescence enhancement*

Monolayer TMDs with their direct bandgap, mechanical flexibility and versatility for chemical functionalization are promising material for ultrathin optoelectronic applications such as photodetectors, optical sensors, solar cells, and light-emitting devices.[1−3] Recent advancement in wafer-scale growth shows the possibility of scalable optoelectronic applications for MoS_2.[4−6] Among various synthesis techniques, metal–organic chemical vapor deposition (MOCVD) is the most promising approach to obtain wafer-scale transition metal dichalcogenides (TMDs). MOCVD provides the advantage of a back-end-of-line (BEOL) compatible process, and many efforts are ongoing to improve the method, mainly for minimizing amorphous carbon contamination and reducing the reaction temperature.[7−10] As new growth techniques evolve, the postprocessing of films grown by different methods also becomes a crucial issue for integrating MOCVD-TMDs into devices.

As an archetype on group-6 semiconducting TMD, MoS_2 stands out as one of the most promising candidates for both ultrathin electronic and optoelectronic applications including photodetector and light-emitting diodes (LED).[11−14] In addition, the photoluminescent property of MoS_2 enabling *in situ* monitoring of chemical redox interactions or catalytic reactions on its surface, including hydrogen evolution reaction (HER).[15,16] However, they typically show extremely low photoluminescence quantum yield (PLQY), reported as less than 1% in ambient conditions, due to the trion-based exciton

Received: May 28, 2025
Revised: September 5, 2025
Accepted: September 9, 2025
Published: September 25, 2025

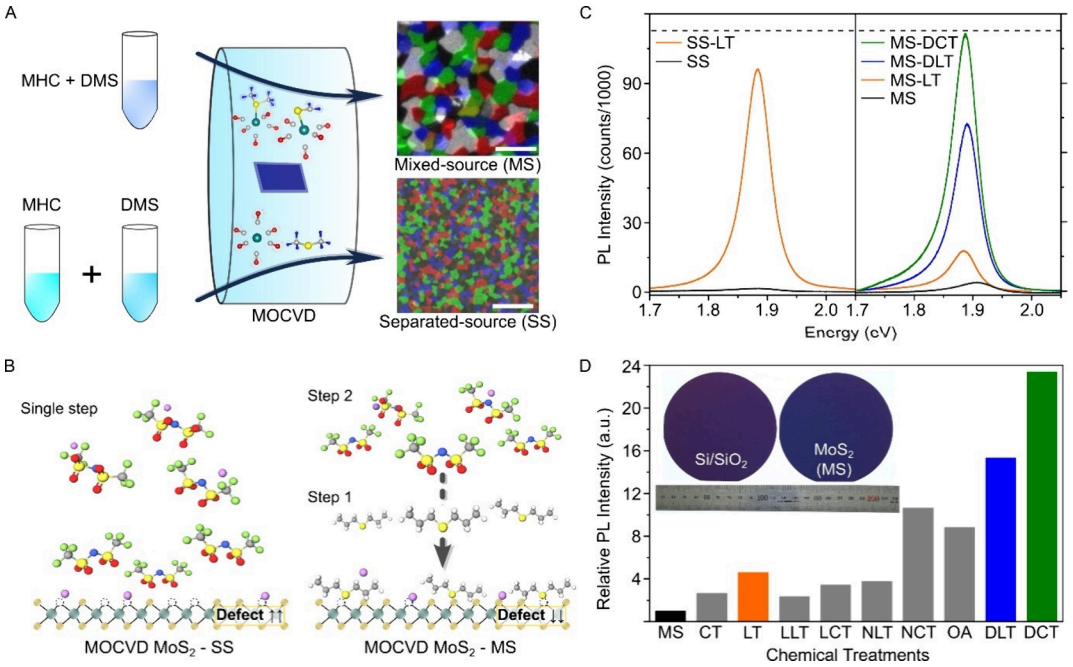

Figure 1. Chemical treatment for photoluminescence (PL) enhancement of MOCVD-grown MoS_2. A. Schematic of two growth methods and dark-field transmission electron microscopy (TEM) images from each growth condition. Scale bar for the inset figures: 2 μm. B. Schematics of chemical treatment for MOCVD-grown monolayer MoS_2, grown with two different method. MOCVD-MoS_2 film named SS has grown with separated sources, and the film MS has grown with mixed-source. Single Li-TFSI treatment works for SS film (higher defect density) and dual chemical treatment process of dipropyl sulfide (DPS) followed by Li-TFSI works for MS film (lower defect density). C. Representative PL spectra for untreated (SS, MS), Li-TFSI treated (SS-LT, MS-LT), and dual-step chemical treated (DPS followed by Li-TFSI/$Ca(TFSI)_2$ denoted to MS-DLT, MS-DCT) MOCVD-MoS_2 samples, measured at an excitation power of approximately 5×10^2 W cm^{-2}. The dashed line is an instrumental detection limit. D. General illustration of PL enhancements on MS film by different chemical treatments. PL intensity was normalized to the intensity of the pristine sample (MS). (CT: $Ca(TFSI)_2$, LT: Li-TFSI, LLT/LCT: Li_2S followed by Li-TFSI/$Ca(TFSI)_2$, NLT/NCT: Na_2S followed by Li-TFSI/$Ca(TFSI)_2$, OA: Oleic acid, DLT/DCT: dipropyl sulfide(DPS) followed by Li-TFSI/$Ca(TFSI)_2$ treated). Inset images show 4 in. growth of MS-MoS_2 films on Si/SiO_2 wafers.

quenching and various nonradiative recombination pathways induced by defects.[17−20] Numerous efforts have been made to understand the nature of the radiative recombination process and identified effects from atomic defects, electron doping, excessive electrons on the surface, and substitute atoms on various TMDs.[19,21−26] Monolayer TMDs have several different classes of defects.[27−30] For example, MoS_2 grown by chemical vapor deposition (CVD) exhibits numerous defects depending on the particular growth method, including single-atom vacancies originating from nonuniform vapor pressure and line defects such as grain boundaries due to the insufficient nucleation density and random crystal orientation during the growth process.[31−34] Therefore, a systematic approach is required to build a strategy for enhancing the PL of MoS_2 using novel growth methods.

Chemical treatment or electrostatic doping has been employed as one method to control the surface electrons or trion population to enhance the PL intensity of TMDs. The treatment involving *p*-dopants or negative-bias in field effect doping reduce the surface electron density and trion-mediated nonradiative processes.[18,35−43] Among chemical approaches, H-TFSI (bis(trifluoromethane)sulfonimide) and Li-TFSI (lithium bis(trifluoromethylsulfonyl)imide) treatments on mechanically exfoliated TMDs show very large PL enhancements.[26,44−46] Additionally, thiol-analogues have been introduced to address sulfur defects by filling sulfur vacancies.[47,48] Both chemical approaches or combined methods passivate the defects and neutralize the surface, thereby increasing the population of neutral excitons and enhancing PL in MoS_2 prepared by either mechanical exfoliation or CVD.[44,48,49]

Here, we report the first investigation (to the best of our knowledge) into chemical treatment on wafer-scale monolayer MoS_2 films, with the effect of chemical passivation being strongly influenced by the underlying MOCVD growth methodology. By a thorough understanding of the characteristics of defects, doping, and action of the passivating chemicals, it is possible to design rational passivation routes that enhance the PL of wafer-scale MOCVD grown films by levels similar to PL enhancement achieved in mechanically exfoliated MoS_2 flakes (23−50×).

RESULTS AND DISCUSSION

We studied wafer-scale (4-inch) MoS_2 film grown by two different MOCVD methods − (1) using separated precursor source (SS) of transition metal and chalcogen, or (2) using mixed precursor source (MS), see Figure 1A. Conventionally, the SS method has been used for MOCVD growth of TMDs. However, amorphous carbon contamination is a major concern. Although chalcogen-hydride gases (i.e., H_2S, H_2Se) have been used to address these issues, requiring a high-temperature process (i.e., 1000 °C) makes them incompatible with back-end-of-line integration. Additionally, the hydrides are extremely toxic, thus causing the high cost for rigorous safety, which is another drawbacks.[50,51] The MOCVD method utilizing the MS approach converts from individual precursors to ligands that contain both Mo and S elements, thus providing

https://doi.org/10.1021/acsnano.5c08927
ACS Nano 2025, 19, 34698−34707

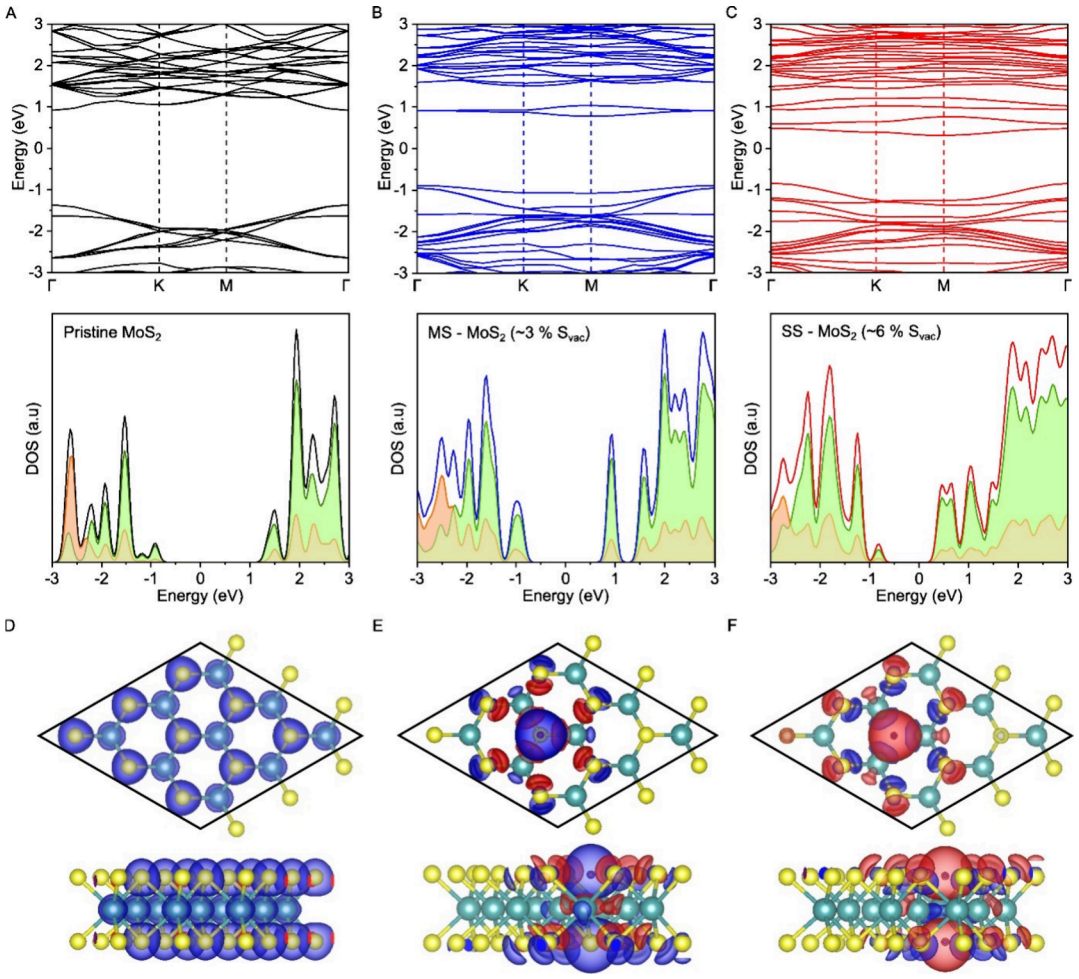

Figure 2. Band energy and DOS of pristine MoS_2, and MoS_2 with lower defect density and higher defect density. A-C. Band energy and density-of-state of pristine MoS_2, low sulfur vacancies MoS_2, and high sulfur vacancies MoS_2, respectively. (At the lower column, green shaded: partial DOS of Mo atoms; orange shaded: partial DOS of S atoms; black, blue, and red lines represent the total DOS.) D-F. Partial charge density isosurfaces of pristine MoS_2, low S_{vac} MoS_2, and high S_{vac} MoS_2 surfaces.

a new pathway to minimal amorphous carbon formation while keeping the advantage of a low-temperature process (i.e., 600 °C). The MoS_2 film obtained by the MS approach shows improved uniformity and reduced defect density, which suppresses *n*-doping compared to the sample obtained by the SS method, as has been shown before.[6,52] In both methods, molybdenum hexacarbonyl (MHC) and dimethyl sulfide (DMS) are used as precursors for molybdenum and sulfur, respectively. In contrast to H_2S, DMS is less toxic and, therefore, garners the attention of the industry. In addition, the use of DMS allows minimization of the gas-phase parasitic reaction that can affect the uniformity and quality of TMDs. In the separated-source (SS) method, MHC is kept in its original solid form, creating an unstable flux. This results in an undesirable nonuniform nucleation distribution, leading to small grain size and variations in quality among different batches. In contrast, the mixed-source (MS) method provides a controllable way to introduce Mo flux by dissolving MHC in DMS, which creates the $Mo(CO_5)((CH_3)_2S)$ ligand.[52] Therefore, this approach enables the modulation of nucleation density and leads to larger grain size. We measured the grain size of each growth method by dark-field TEM imaging using JEM-2100Plus (JEOL) system operated at 200 kV.[6] The dark-field TEM images on the right side of Figure 1A clearly depict the different grain sizes of films from the two methods. SEM images taken during growth also demonstrate the larger grain sizes of the MS method (Figure S3). Importantly, the MS method promotes MoS_2 growth dominantly on the substrate, eliminating the formation of amorphous carbon contamination, which is a primary concern in the MOCVD process (detailed explanation of the thermodynamics of the growth method is provided in Figure S4). The use of the MS method for the MOCVD process provides a better MoS_2 quality (i.e., amorphous carbon-free, low sulfur vacancies, and reduces the number of grain boundaries), bringing MoS_2 closer to practical application.[53]

Figure 1B illustrates the generic scheme for the chemical treatment process on the MOCVD-MoS_2 films in this study. All chemical treatment processes are conducted post growth, with the chemicals delivered to the films via the solution phase. As we develop below, the different growth methods require distinct chemical treatment approaches for enhancing PL. While the single Li-TFSI treatment enhances the PL of SS film, a dual-step sequential chemical treatment with dipropyl sulfide (DPS) followed by Li-TFSI enhances the PL of MS film to a similar level of Li-TFSI treated SS sample.

Figure 1C shows the PL spectra of each (SS, MS) when untreated and treated. To ensure reliable and repeatable

https://doi.org/10.1021/acsnano.5c08927
ACS Nano 2025, 19, 34698−34707

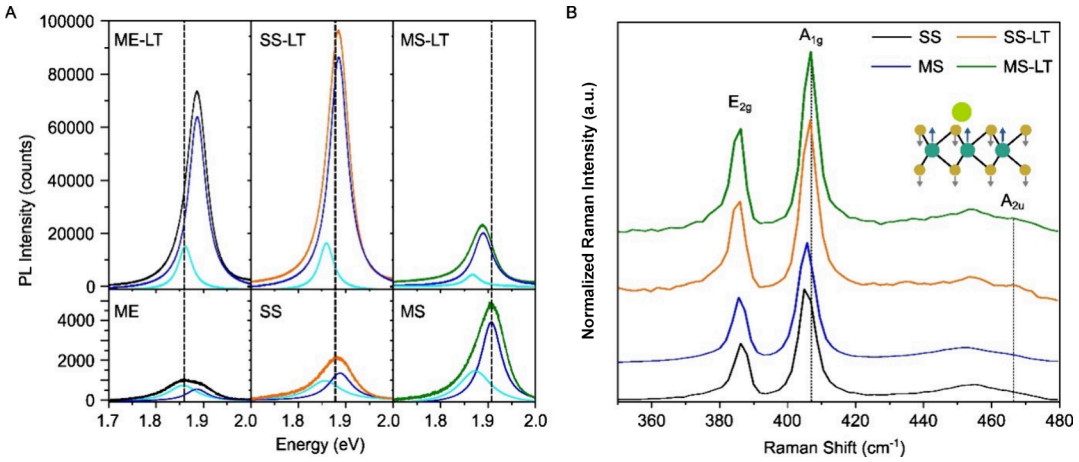

Figure 3. Li-TFSI treatment on MoS_2. A. PL spectra of the untreated sample (ME for mechanically exfoliated, or SS, MS for as transferred sample, in bottom raw) and Li-TFSI treated (top raw) of each MoS_2. All spectra deconvoluted by trion (cyon) and neutral exciton (blue) peaks. B. Raman spectra of Li-TFSI treated MoS_2 in A. Inset image shows the Raman A_{2u} mode of MoS_2.

measurements with a high signal-to-noise ratio, the excitation density and integration time were fixed for all measurements (see experimental methods for details). This allows for an accurate comparison of PL counts between different samples and treatment conditions. For the SS sample (left column), a single Li-TFSI treatment enhanced PL up to 49× (SS-LT), which is comparable to the previous reports using mechanically exfoliated samples.[44] The MS sample (right column) having a lower defect density and larger grain size (details in Figure 1A) exhibits higher intrinsic PL intensity. However, the effect of a single Li-TFSI treatment on the MS sample (MS-LT) is around 3.5×, which is much lower than the effect for the SS sample. This was improved to 15× by pretreatment of DPS (MS-DLT) and further enhanced to 23× by dual-step treatment of DPS and $Ca(TFSI)_2$ (MS-DCT), giving a final PL intensity comparable to the intensity of Li-TFSI treated SS samples (MS-LT) (see experimental methods for details on treatment protocols). This highlights the intrinsic difference in the nature of the MoS_2 film arising from different growth methods, which require distinct chemical treatment strategies for PL enhancement. The PL of the SS sample becomes brighter with a dual-step treatment of DPS followed by $Ca(TFSI)_2$ (Figure S2), while the effect of DPS pretreatment is more noticeable in the MS sample. When the domains coalesce, line defects can form, causing localized strain that impacts the band energy of the MoS_2 film.[54,55] As a result, variations in the defect density could lead to differences in the shifting direction of the PL peak position after chemical treatment.

Figure 1D shows the PL enhancement for MS-MoS_2 films using various chemical treatment protocols. We studied the effect of inorganic compounds (lithium sulfide (Li_2S), sodium sulfide (Na_2S)) and dipropyl sulfide (DPS) as a prepassivation agent, and Li-TFSI and $Ca(TFSI)_2$ as *p*-doping agents. Additionally, we also tried oleic acid (OA) as a mild *p*-doping agent.[43] (All chemicals are introduced in Figure S1.) The DPS treatment followed by Li-TFSI and $Ca(TFSI)_2$ shows the most significant PL enhancement for MS-MoS_2. The inset figure depicts the 4 in. growth of MS-MoS_2 film on Si/SiO_2 wafer. The film exhibits uniformity, in both mechanical and optical characterization conducted through AFM, PL spectra, and Raman spectra measurements. Additionally, the transient absorption spectra indicate negligible defect-mediated low-energy transitions (Figures S5−S6).

To understand the difference in defects and doping between the SS and MS grown films, we turned to density functional theory (DFT). Figure 2 shows the energy bands and density of states (DOS) of three different types of MoS_2: pristine, with lower sulfur vacancies (3% S_{vac}, comparable to MS), and with higher S_{vac} (6% S_{vac}, comparable to SS). The analysis of the partial density of states (PDOS) indicates that the pristine MoS_2 has a band gap of approximately 1.81 eV, consistent with previous density functional theory (DFT) studies and experimental observations.[56−58] In the presence of sulfur vacancies (S_{vac}), midgap states are induced within the MoS_2 bandgap. These new states act as local or transition states between the valence band maximum (VBM) and conduction band minimum (CBM). These new midgap states induced by sulfur vacancies cause a stronger *n*-doping effect at higher S_{vac} concentrations. This shows the intrinsic doping nature is different depending on different growth methods and implicate different chemical treatments on the surface would be necessary for enhancing the PL.

Figure 3A presents the PL spectra of untreated and Li-TFSI treated MoS_2 prepared by three different methods: mechanical exfoliation (ME), MOCVD-SS, and MOCVD-MS. Before the treatment (lower panel), the MS sample exhibits the highest PL intensity with a blue-shifted peak position (1.9 eV) which is attributed to the emission of the neutral-exciton,[18,59] while the ME and SS film show lower PL intensity and a PL peak at lower energy (around 1.87 eV) attributed to higher trion concentrations resulting from higher concentration of sulfur vacancy and grain boundaries. The Li-TFSI treatment enhanced the PL intensity of both ME and SS samples by approximately 50×, inducing a blue-shift in the PL peak by around 0.1 eV. This indicates that Li+ cation works as *p*-dopants, reducing the trion concentration and enhancing the PL, consistent with previous study[44] (Table S1). However, for the MS sample, the PL enhancement is modest (3.5×), and the PL is red-shifted by around 0.11 eV. The PL intensity is uniformly distributed both before and after Li-TFSI treatment, and the intensity trend between ME, SS, and MS remains consistent with multiple measurements with different films or spots (Figure S7−8).

https://doi.org/10.1021/acsnano.5c08927
ACS Nano 2025, 19, 34698−34707

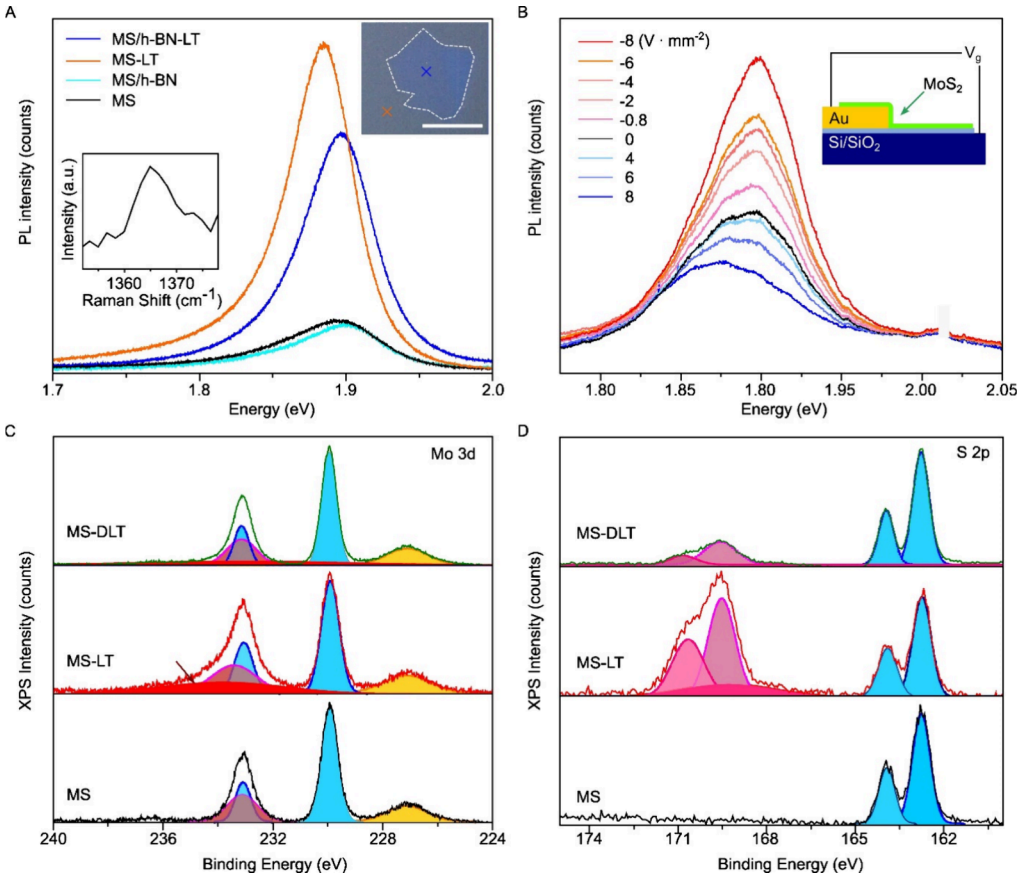

Figure 4. Li-TFSI treatment on MS-MoS_2. A. PL spectra of h-BN covered the MS film. The inset graph shows the Raman spectra of h-BN. The inset image shows an optical image of the h-BN covered region, and the arrow shows the measurement point (blue: h-BN covered MS-MoS_2, orange: uncovered MS-MoS_2) B. Electrostatic PL modulation. Inset image shows the measurement schematic. C–D. XPS spectra of untreated (MS), Li-TFSI only treated MS-MoS_2 (MS-LT), and DPS followed by Li-TFSI treated MS-MoS_2 (MS-DLT) C. Mo 3d, and D. S 2p.

Figure 3B presents the Raman spectra of untreated and Li-TFSI-treated MOCVD-MoS_2 samples (SS, MS). The major Raman modes, including in-plane $E_{2g}{}^1$ mode at around 388 cm^{-1}, and A_{1g} mode at around 405 cm^{-1} are observed for all untreated or treated samples (MS, SS).[60] It is shown that the E_{2g} peaks of SS and MS samples are located at 405.59 and 404.83 cm^{-1}, respectively, which presents both samples showing comparable strain properties in the constructed ε-n space within the Pos(A_{1g}) vs Pos(E_{2g}) plot of within the standard deviation of exfoliated MoS_2 (Figure S9).[60] With Li-TFSI treatment, the A_{1g} mode blue-shifts to 407 cm^{-1} with a new Raman A_{2u} mode at 468 cm^{-1} emerging for both SS and MS samples (Figure S10). The A_{1g} Raman mode is sensitive to electron doping, and the A_{2u} mode originates from non-symmetry due to the presence of cations.[44] Therefore, it is plausible that the interactions between the lithium cation and the MoS_2 surface are similar in both samples, consistent with a previous study. Similar Raman spectra were measured at $Ca(TFSI)_2$ treatment (Figure S11). However, the other role of Li-TFSI emerges in the MS sample, a modest enhancement and a red-shift of PL peak, suggesting that although the general methodology of chemically driven PL enhancement has similar effects, the different nature of defects in films grown using different methods could lead to varied effects on the material, demanding a tailored study for different growth methods.

In Figure 4A, we investigated the effect of Li-TFSI on the MS-MoS_2 surface by stacking a thin layer of mechanically exfoliated hexagonal boron nitride (h-BN) on top of the MoS_2. The h-BN layer has a thickness of around 5–6 layers from the peak position of Raman spectra (1364.5 cm^{-1}) (full Raman spectra presented in Figure S12).[61] The MoS_2 area covered by h-BN (blue spot in the inset in Figure 4A) exhibited comparable PL intensity and peak position but a narrower full width at half-maximum (FWHM) of the peak compared to the noncovered MoS_2 (orange spot in the inset in Figure 4A). The thin layer of h-BN serves to protect the surface of MoS_2 while allowing remote charge transfer doping through the h-BN flake, from the chemical dopants on the topmost surface to the MoS_2 beneath.[62] We observed enhanced and red-shifted PL when from the Li-TFSI treatment on a bare spot (orange spot/spectra), similar to Figure 3A. However, the red-shift was suppressed in the presence of h-BN on top, while PL was still enhanced (blue spot/spectra).

In Figure 4B, we employed electrostatic gating to modulate PL properties by controlling the background doping.[18,59] We transferred MS-MoS_2 on SiO_2 (300 nm)/Si^{++} substrate with prepatterned Au electrode and measured PL with controlling the bias voltage (V_g). The PL intensity decreased and red-shifted (from 1.9 to 1.88 eV) when $V_{GS} > 0$ V, while it increased and slightly blue-shifted when $V_{GS} < 0$ V. This result is consistent with previous reports,[18,59] showing that the existence of a controllable background electron concentration on the MS sample can enhance the PL intensity by *p*-dopants, albeit accompanied by a very small blue-shift of PL peak position. Therefore, the red-shift observed in the PL spectra from the Li-TFSI treatment, in contrast to the consistent peak

https://doi.org/10.1021/acsnano.5c08927
ACS Nano 2025, 19, 34698–34707

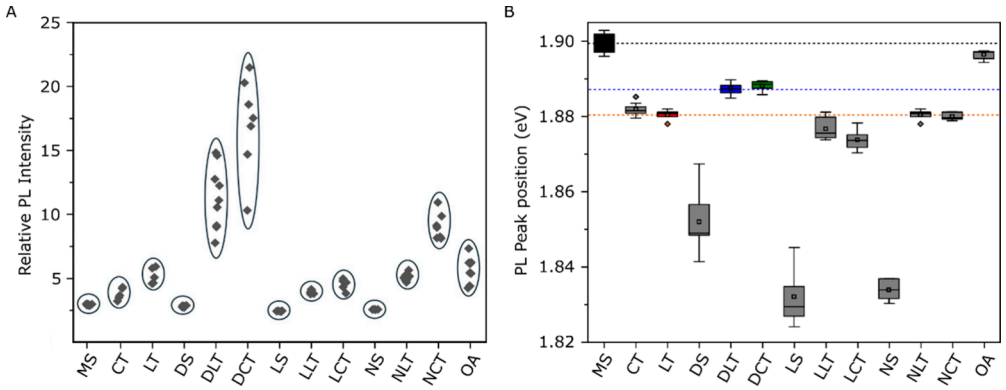

Figure 5. Statistics of various chemical treatments on MS-MoS_2. A. PL intensity B. PL peak position.

positions observed in the electrostatic gating or h-BN encapsulation experiments, suggests that the direct treatment of Li-TFSI on the surface may induce other effects on the MS-MoS_2 surface that lead to the red-shifting of the PL peak. This aligns with oleic acid (OA) treatment, which is a simple long-chain acid known to be a weak acid to stabilize colloidal quantum dots by passivating dangling bonds. It has been reported while OA may not effectively protonate the monolayer TMD surface compared to Li-TFSI/$Ca(TFSI)_2$, it can reduce *n*-doping by passivating sulfur vacancies.[43,63] In Figure S13, the treatment with OA exhibits a comparable enhancement in PL intensity to the Li-TFSI treatment while it did not result in a red-shift of the PL peak. Furthermore, we measured PL lifetime to compare the effect of DPS, Li-TFSI, and $Ca(TFSI)_2$ (Figure S14). The DPS treatment shows a shorter or very similar PL lifetime, while both Li-TFSI and $Ca(TFSI)_2$ treatments result in a longer lifetime, suggesting a trap-mediated exciton recombination process.[19,49] This longer lifetime differs from the Li-TFSI treatment on exfoliate MoS_2, which exhibited a shorter PL lifetime.[44] DPS and thiol analogues including 2-furanmethanothiol (FSH) molecule passivate trap states.[44,46,49] These results highlight the positive role of DPS in MS samples and suggest that the choice of chemicals should be carefully considered, not only for doping control but also for passivating various types of defects and trap states.[64]

In Figure 4C−D, we present X-ray photoelectron spectroscopy (XPS) analysis for Li-TFSI treated and DPS followed by Li-TFSI treated MS samples measured by ultrahigh-vacuum photoemission instrument (Escalab 250Xi). In the Mo 3d XPS spectra in Figure 4C, while three peaks from MoS_2 (Mo 3d 3/2:232.9 eV, Mo 3d 5/2:229.8 eV, S 2s: 227.2 eV) appear, we observe another signal around 235.4 eV, which indicates the presence of oxidation with single Li-TFSI treatment.[7,65−67] This oxidation is suppressed by prior DPS treatment. The XPS spectra of the S 2p in Figure 4D shows the signal from MoS_2 (S 2p 1/2:164 eV, S 2p 3/2:162.8 eV) with the doublets of the TFSI anion at 169, 170.2 eV.[68,69] Similar TFSI anion peaks are observed with $Ca(TFSI)_2$ treatment, and F 1s spectra show the presence of TFSI anion after LiTFSI treatment (Figure S15−16). The peak intensity for the TFSI residue on the surface is decreased at prior DPS treatment. The Li 1s signal in Figure S15 shows that lithium remains on MoS_2 after both Li-TFSI and DPS followed by Li-TFSI treatment.[70] However, it is challenging to confirm whether the physically adsorbed lithium forms a Li−S chemical bond or remains on the MoS_2 surface and is oxidized during the measurement process. Our previous studies show that Li-TFSI cannot alter the electronic structure of WS_2, and a divalent sulfur coordination is needed for effective defect passivation when the defects are neutral sulfur vacancies instead of charged defects.[46] We propose that MS-MoS_2 exhibits a reduced overall vacancy concentration with a lower proportion of charged sulfur vacancies from the favorable thermodynamics for the growth (Figure S4) and higher PL intensity with a blue-shifted energy (Figure 3A). As a result, the proportion of neutral defects would be higher at MS-MoS_2. Accordingly, a sequential dual-passivation strategy employing dipropyl sulfide (DPS) followed by Li-TFSI treatment leads to more effective PL enhancement, consistent with our previous study.[46] In contrast, SS-MoS_2, which has a higher density of defects including both charged and neutral vacancies, responds well to Li-TFSI treatment alone, primarily due to its *p*-doping effect.[44]

Figure 5 presents the statistics of various chemical treatments on MS-MoS_2 (original PL and Raman spectra of Li_2S and Na_2S treatment presented in Figure S17). We note that one to two points were measured per sample, and an untreated reference sample was measured alongside to ensure consistency. In the case of Li_2S and Na_2S, dual treatment is involved, both Li_2S and Na_2S have a strong tendency to undergo hydrolysis, forming strongly alkaline solutions. The significant red-shift observed is due to the formation of negative trion. The minimal effect of the Li_2S followed by Li-TFSI treatment supports our hypothesis that divalent sulfur species are necessary for Li^+ coordination. The overall trend of PL enhancement and peak shift remains consistent with Figure 1D, while the PL intensity in Figure 5A presents variation of up to 25% (Figure S20). We note that statistics of chemical treatments have generally not been well reported in the literature to date. Here, we present the statistics of each treatment to provide a guide for their reproducibility. A previous study has shown that TFSI-based salts with different cations (Cu^{2+}, Mg^{2+}, Ca^{2+}, Na^+, K^+) exhibit similar PL enhancement, indicating a negligible correlation between cationic radii and PL tuning strength. However, we note, for instance, that when applying $Ca(TFSI)_2$, a divalent cation based ionic salt, the variation is higher than other treatments. This can be attributed to its lower ionic mobility compared to that of the Li^+ ion. In Figure 5B, we compare the positions of the PL peaks. When we treated MoS_2 with TFSI-based ionic salts, the red-shift became more prominent, while DPS treatment suppressed this red-shift. This variation may also be related to long-term stability, including air exposure during the measurement. Therefore, further studies investigating the

https://doi.org/10.1021/acsnano.5c08927
ACS Nano 2025, 19, 34698−34707

stability of the treated films under conditions such as the treatment parameter, humidity, elevated temperature, and mechanical strain would be expected. Similar chemical passivation strategy is applicable to various TMDs, including $MoSe_2$ and WS_2. For WS_2, both Li-TFSI and sequence-specific treatments enhance PL and mobility.[43,46,63,71] Our findings regarding MOCVD-grown MoS_2 suggest its broader applicability across TMDs with diverse growth methods.

CONCLUSION

In summary, we investigated surface chemical treatment protocols to enhance the PL yields of wafer-scale MOCVD-grown monolayer MoS_2. We showed that for MOCVD-MoS_2 grown via the conventional separate source route, which results in higher defect densities and higher *n*-doping, TFSI-based ionic salt chemical treatment can greatly enhance the PL intensity. In contrast, MOCVD-MoS_2 grown via the mixed source route, which shows lower defect densities with more neutral sulfur vacancies, does not respond as well to the TFSI-based chemical treatment. For these materials, we developed a dual-step chemical passivation strategy, providing an effective neutral defects passivation with the coordination between thiol and Li^+. This led to a 23-fold improvement in PL yield from MOCVD-MoS_2. Our results show that chemical treatment protocols to passivate defects and improve PL yield, which have so far been studied on exfoliated and CVD samples, can also be applied to wafer-scale MOCVD-grown materials. Furthermore, we presented design rules for how to tune chemical treatment procedures, depending on the defect densities and doping levels of the underlying materials, allowing for successful passivation and large PL enhancements across the board.

METHODS

MOCVD Growth and Transfer. We used a home-built multiple heating zones MOCVD system to synthesize continuous monolayer MoS_2 films. A 4 in. Si wafer with a 300 nm-thick SiO_2 layer was cleaned with diluted hydrofluoric acid (HF: H_2O = 1:20 v/v), deionized water, isopropyl alcohol, and dried with N_2 gas before being placed into the MOCVD chamber. Molybdenum hexacarbonyl (MHC, MilliporeSigma 577766) and dimethyl sulfide anhydrous (DMS, MilliporeSigma 274380) were used as the Mo- and S-based precursors for the synthesis. For the separated-source method, 0.5 sccm MHC and 0.3 sccm DMS were injected independently into the chamber for 22 h. For the mixed-source method, 65 mg of MHC was dissolved entirely in 15 mL of DML. The mixture was then precisely injected into the chamber in two steps: starting with 1.0 sccm for 16 h, followed by an increase to 1.7 sccm for 6 h. A combination of 310 sccm Ar and 5 sccm H_2 was used as a carrier gas for both methods to achieve a fully coalesced monolayer MoS_2.

A thin layer of poly(methyl methacrylate) (PMMA) was spin-coated on the top of the MOCVD-MoS_2 film for the wet-transfer process. MoS_2 films on Si/SiO_2 were cut into appropriate sizes and floated on deionized (DI) water. Within an hour, the Si/SiO_2 substrates detached from the MoS_2/PMMA and submerged, while the MoS_2/PMMA remained floating on the DI. This separation occurs due to the difference in hydrophilicity between the SiO_2/MoS_2 interface and the existence of the ionic sacrificial layer. Next, using the "scooping up" method, we transferred the floating MoS_2/PMMA film onto the glass substrate. The samples were then carefully dried on a hot plate overnight and placed under vacuum for several hours to enhance adhesion. Finally, the PMMA layer was removed by washing the samples with sufficient amounts of acetone and isopropanol (IPA).

Sample Preparation. *Mechanical Exfoliation.* We mechanically exfoliated MoS_2 and h-BN using a PDMS-assisted method. First, we roughly exfoliated MoS_2 crystal (2D semiconductor) and h-BN crystal using blue tape (Ultron systems) and then transferred them to the PDMS film. Flakes with suitable size, thickness (monolayer MoS_2 and very thin-layered h-BN) and shape were identified and transferred onto designated substrates (thin glass substrate (170 μm thickness, Thorlab) or Si/SiO_2 substrate with 300 nm SiO_2. The monolayer MoS_2 was confirmed by measuring the PL spectra.

Transfer of MOCVD-MoS_2 (MS, SS). The transfer is done by DI mediated wet-transfer.

Chemical Treatment. We made and treated each chemical for chemical treatment studies following the procedures. All treatments were conducted in a nitrogen glovebox to ensure an inert environment. In the case of the dual-step treatment, we did the first chemical treatment, fully dried the sample, and then completed the second chemical treatment.

Li-TFSI and Ca(TFSI)$_2$. The solid form of each Li-TFSI and $Ca(TFSI)_2$ salt was bought from Sigma-Aldrich. Each salt dissolved in Methanol (Sigma-Aldrich) at a concentration of 5 mg/mL. The chemical treatment of MoS_2 has been done by immersing the whole sample for 30 min, followed by drying, mild washing using Methanol (for removing excessive chemicals), and the sample was fully dried. All treatments were conducted in a nitrogen glovebox to ensure an inert environment.

Dipropyl Sulfide (DPS). A 0.1 M solution of dipropyl sulfide was prepared by dissolving dipropyl sulfide powder in 1,2-dichloroethane solvent (Both from Signal Aldrich). We note that 1,2-dichloroethane (DCE) is a nonpolar medium known for its effectiveness in dispersing MoS_2 nanosheets without inducing additional sulfur vacancies.[72] Previous reports have shown that DCE may lead to mild *n*-type doping, as Cl atoms incorporated into sulfur vacancies, which may explain the slight red-shift observed in PL (Figure 1C).[73] However, our data indicate that DPS treatment results in defect passivation rather than defect formation.

MoS_2 sample was immersed in the prepared solution for 1 day. Then, sample went through mild washing using 1,2-dichloroethane, and dried. All processes were conducted inside the glovebox.

Na_2S, Li_2S. We made 0.1 M Na_2S and Li_2S solution by dissolving each salt (Signal Aldrich) in a methanol solvent. Treatment was done by immersing the sample for 1 day followed by gentle washing using methanol and drying in the nitrogen glovebox.

OA. Oleic acid (OA) has been used following the experimental procedure in a previous study.[43]

Optical Characterization. The steady-state PL and Raman measurements were performed under ambient conditions by using a Renishaw inVia Raman microscope. The excitation laser source with a wavelength of 532 nm was utilized for both PL and Raman measurements. Prior to conducting any measurements, the spectrometer was calibrated using a silicon reference sample to correct for instrument responses and having a stable initial count to the silicon wafer.

Each treated sample was stored in a nitrogen-filled glovebox for less than 2 weeks and subsequently measured under ambient conditions. Each sample was exposed to air for less than 6 h during measurement. The PL enhancement remained consistent throughout this period, indicating that short-term exposure to air does not significantly compromise the treatment's efficacy. This suggests that the treatment maintains reasonable stability under typical laboratory conditions.

During the measurements, the laser power was set to 0.05% (<0.5 μW) and focused onto the specific point of the flake using a 20× long working distance objective (NA = 0.40). The FWHM of the excitation beam is 678.3 nm, calculated using the NA (0.40) and excitation wavelength (532 nm). From the dark-field TEM image, we can postulate that we are collecting data from 4 to 5 grains of MS sample, and 9−10 grains of SS samples. The emitted light was collected in streamline mode and dispersed by a 1800 l/mm grating.

The time-resolved PL lifetime was measured by using a custom-built optical microscope setup. Excitation was provided by filtering white light using a 532 ± 10 nm band-pass filter. PL lifetimes were measured using TCSPC electronics after filtering out using a 660 ± 10 nm band-pass filter.

https://doi.org/10.1021/acsnano.5c08927
ACS Nano 2025, 19, 34698−34707

Quantum Chemical Calculations. DFT calculations for gas-phase reactions were carried out using the Gaussian 16 suite of programs.[74] The geometries of molecular precursors were optimized by using the B97D3 functional with a def2-tzvp basis set, except for Mo for which LANL2DZ pseudopotential was assigned. For the calculation of the Gibbs free energy values, a temperature of 700 °C and a pressure of 10 Torr were assumed.

DFT calculations for the MoS_2 slab models were performed using Vienna ab initio simulation (VASP)[75] package version 5.4.4. The monolayer of MoS_2 with vacuum space of 15Å was used for calculations. For structural relaxation, the PBE functional[76] with D3BJ dispersion correction[77] was applied using projector-augmented wave methods. A cutoff energy of 350 eV and a 2 × 2 × 1 Monkhorst−Pack k-point mesh were used for relaxation and self-consistent calculations. For the PBE-optimized geometries, the projected density of state (PDOS) and band gap were obtained using HSE06 hybrid functional[78] and a 9 × 9 × 1 Monkhorst−Pack k-point mesh.

ASSOCIATED CONTENT

Supporting Information

The Supporting Information is available free of charge at https://pubs.acs.org/doi/10.1021/acsnano.5c08927.

S1: Structure of chemicals used in this study. S2: PL spectrum of dual-step chemical treated SS sample. S3: SEM images of MoS2 domains. S4: Thermodynamics for MOCVD growth. S5: Wafer-scale uniformity of MOCVD MoS2. S6: Optical properties of transferred MoS2 film. S7: Comparison of PL intensity between the exfoliated and MOCVD grown films. S8: PL mapping. S9: Raman fitting. S10−S14: Raman and PL of samples with and without chemical treatment. S15−S16: High resolution XPS scan. S17: PL of samples treated by Li2S and Na2S. S18−S20: Statistic of Raman/PL of samples treated with different chemicals (PDF)

AUTHOR INFORMATION

Corresponding Authors

Jong-Hyun Ahn − *School of Electrical and Electronic Engineering, Yonsei University, Seoul 03722, Republic of Korea;* orcid.org/0000-0002-8135-7719; Email: ahnj@yonsei.ac.kr

Manish Chhowalla − *Department of Materials Science and Metallurgy, University of Cambridge, Cambridge CB3 OFS, U.K.;* orcid.org/0000-0002-8183-4044; Email: mc209@cam.ac.uk

Akshay Rao − *Cavendish Laboratory, University of Cambridge, Cambridge CB3 OHE, U.K.;* orcid.org/0000-0003-4261-0766; Email: ar525@cam.ac.uk

Authors

Juhwan Lim − *Cavendish Laboratory, University of Cambridge, Cambridge CB3 OHE, U.K.; Department of Materials Science and Metallurgy, University of Cambridge, Cambridge CB3 OFS, U.K.;* orcid.org/0000-0003-2597-3012

Anh Tuấn Hoàng − *School of Electrical and Electronic Engineering, Yonsei University, Seoul 03722, Republic of Korea;* orcid.org/0000-0003-0911-1391

Zhaojun Li − *Cavendish Laboratory, University of Cambridge, Cambridge CB3 OHE, U.K.; Department of Materials Science and Engineering, Uppsala University, 75103 Uppsala, Sweden;* orcid.org/0000-0003-2651-1717

Tran Thi Ngoc Van − *Department of Chemical Engineering, Hongik University, Seoul 04066, Republic of Korea;* orcid.org/0000-0003-4214-1103

Jung-In Lee − *Department of Materials Science and Metallurgy, University of Cambridge, Cambridge CB3 OFS, U.K.;* orcid.org/0000-0002-5822-0722

Kihyun Lee − *Department of Physics, Yonsei University, Seoul 03722, Republic of Korea; Center for Nanomedicine, Institute for Basic Science (IBS), Seoul 03722, Republic of Korea;* orcid.org/0000-0003-2468-8447

Nicolas Gauriot − *Cavendish Laboratory, University of Cambridge, Cambridge CB3 OHE, U.K.;* orcid.org/0000-0001-7725-7208

Kyle Frohna − *Cavendish Laboratory, University of Cambridge, Cambridge CB3 OHE, U.K.*

Takashi Taniguchi − *Research Center for Materials Nanoarchitectonics, National Institute for Materials Science, Tsukuba 305-0044, Japan;* orcid.org/0000-0002-1467-3105

Kenji Watanabe − *Research Center for Electronic and Optical Materials, National Institute for Materials Science, Tsukuba 305-0044, Japan;* orcid.org/0000-0003-3701-8119

Bonggeun Shong − *Department of Chemical Engineering, Hongik University, Seoul 04066, Republic of Korea*

Kwanpyo Kim − *Department of Physics, Yonsei University, Seoul 03722, Republic of Korea; Center for Nanomedicine, Institute for Basic Science (IBS), Seoul 03722, Republic of Korea;* orcid.org/0000-0001-8497-2330

Samuel D. Stranks − *Cavendish Laboratory, University of Cambridge, Cambridge CB3 OHE, U.K.; Department of Chemical Engineering and Biotechnology, University of Cambridge, Cambridge CB3 OAS, U.K.;* orcid.org/0000-0002-8303-7292

Complete contact information is available at: https://pubs.acs.org/10.1021/acsnano.5c08927

Author Contributions

[&]J.L. and A.T.H. equally contributed to this work.

Notes

The authors declare no competing financial interest.

ACKNOWLEDGMENTS

This project has received funding from the European Research Council under the European Union's Horizon 2020 research and innovation programme (Grant Agreement No. 758826 (SOLARX) to A.R.). J-I.L, and M.C. acknowledges support from the Faraday Institution LiSTAR programme and characterization project (EP/S003053/1, FIRG014 and FIRG012), NEXGENNA programme (FIRG018), Royal Society Wolfson Merit Award (WRM\FT\180009), and European Research Council (ERC) Advanced Grant under the European Union's Horizon 2020 research and innovation programme (grant agreement GA 101019828-2D- LOTTO). This work was supported by a UKRI Frontier Research Grant (EP/Y015584/1) and by an Engineering Physical Sciences Research Council Programme Grant (EP/W017091/1). For the purpose of open access, the authors have applied a Creative Commons Attribution (CC BY) license to any Author Accepted Manuscript version arising. The data underlying all figures in this article are publicly available from the University of Cambridge repository.

https://doi.org/10.1021/acsnano.5c08927
ACS Nano 2025, 19, 34698−34707

REFERENCES

(1) Chhowalla, M.; et al. The chemistry of two-dimensional layered transition metal dichalcogenide nanosheets. *Nat. Chem.* **2013**, *5*, 263−275.
(2) Manzeli, S.; Ovchinnikov, D.; Pasquier, D.; Yazyev, O. V.; Kis, A. 2D transition metal dichalcogenides. *Nat. Rev. Mater.* **2017**, *2*, 17033.
(3) Mak, K. F.; Lee, C.; Hone, J.; Shan, J.; Heinz, T. F. Atomically thin MoS_2: A new direct-gap semiconductor. *Phys. Rev. Lett.* **2010**, *105*, No. 136805.
(4) Cun, H.; et al. Wafer-scale MOCVD growth of monolayer MoS_2 on sapphire and SiO_2. *Nano Res.* **2019**, *12*, 2646−2652.
(5) Hoang, A. T.; Qu, K.; Chen, X.; Ahn, J. H. Large-area synthesis of transition metal dichalcogenides: Via CVD and solution-based approaches and their device applications. *Nanoscale* **2021**, *13*, 615−633.
(6) Mawlong, L. P. L.; et al. Reduced Defect Density in MOCVD-Grown MoS_2 by Manipulating the Precursor Phase. *ACS Appl. Mater. Interfaces* **2023**, *15*, 47359−47367.
(7) Schaefer, C. M.; et al. Carbon Incorporation in MOCVD of MoS_2 Thin Films Grown from an Organosulfide Precursor. *Chem. Mater.* **2021**, *33*, 4474−4487.
(8) Lin, Y. C.; et al. Realizing Large-Scale, Electronic-Grade Two-Dimensional Semiconductors. *ACS Nano* **2018**, *12*, 965−975.
(9) Hoang, A. T.; et al. Low-temperature growth of MoS_2 on polymer and thin glass substrates for flexible electronics. *Nat. Nanotechnol.* **2023**, *18*, 1439−1447.
(10) Zhu, J.; et al. Low-thermal-budget synthesis of monolayer molybdenum disulfide for silicon back-end-of-line integration on a 200 mm platform. *Nat. Nanotechnol.* **2023**, *18*, 456−463.
(11) Shin, J.-C.; Jeong, J. H.; Kwon, J.; Kim, Y. H.; Kim, B.; Woo, S.-J.; Woo, K. Y.; Cho, M.; Watanabe, K.; Taniguchi, T.; et al. Electrically Confined Electroluminescence of Neutral Excitons in WSe_2 Light-Emitting Transistors. *Adv. Mater.* **2024**, *36*, 1−8.
(12) Palacios-Berraquero, C.; Barbone, M.; Kara, D. M.; Chen, X.; Goykhman, I.; Yoon, D.; Ott, A. K.; Beitner, J.; Watanabe, K.; Taniguchi, T.; et al. Atomically thin quantum light-emitting diodes. *Nat. Commun.* **2016**, *7*, 12978.
(13) Im, H.; Kim, J.; Kim, J.; Kim, S. Scalable Bilayer MoS_2-Based Vertically Inverted p−i−n Light-Emitting Diodes. *Adv. Mater. Interfaces* **2024**, *11*, 2300319.
(14) Lim, J.; et al. Photoredox phase engineering of transition metal dichalcogenides. *Nature* **2024**, *633*, 83−89.
(15) Reynolds, M. F.; Guimaraes, M. H. D.; Gao, H.; Kang, K.; Cortese, A. J.; Ralph, D. C.; Park, J.; McEuen, P. L. MoS_2 pixel arrays for real-time photoluminescence imaging of redox molecules. *Sci. Adv.* **2019**, *5*, 2−10.
(16) Hsiao, F. H.; et al. Using Exciton/Trion Dynamics to Spatially Monitor the Catalytic Activities of MoS_2 during the Hydrogen Evolution Reaction. *ACS Nano* **2022**, *16*, 4298−4307.
(17) Kim, H.; Uddin, S. Z.; Higashitarumizu, N.; Rabani, E.; Javey, A. Inhibited nonradiative decay at all exciton densities in monolayer semiconductors. *Science* **2021**, *373*, 448−452.
(18) Lien, D. H.; et al. Electrical suppression of all nonradiative recombination pathways in monolayer semiconductors. *Science.* **2019**, *364*, 468−471.
(19) Goodman, A. J.; Willard, A. P.; Tisdale, W. A. Exciton trapping is responsible for the long apparent lifetime in acid-treated MoS_2. *Phys. Rev. B* **2017**, *96*, 121404.
(20) Shen, P. C.; et al. Healing of donor defect states in monolayer molybdenum disulfide using oxygen-incorporated chemical vapour deposition. *Nat. Electron.* **2022**, *5*, 28−36.
(21) Shi, H.; et al. Exciton dynamics in suspended monolayer and few-layer MoS_2 2D crystals. *ACS Nano* **2013**, *7*, 1072−1080.
(22) Yuan, L.; Huang, L. Exciton dynamics and annihilation in WS_2 2D semiconductors. *Nanoscale* **2015**, *7*, 7402−7408.
(23) Mitterreiter, E.; Schuler, B.; Micevic, A.; Hernangomez-Perez, D.; Barthelmi, K.; Cochrane, K. A.; Kiemle, J.; Sigger, F.; Klein, J.; Wong, E.; et al. The role of chalcogen vacancies for atomic defect emission in MoS_2. *Nat. Commun.* **2021**, *12*, 1−8.
(24) Refaely-Abramson, S.; Qiu, D. Y.; Louie, S. G.; Neaton, J. B. Defect-Induced Modification of Low-Lying Excitons and Valley Selectivity in Monolayer Transition Metal Dichalcogenides. *Phys. Rev. Lett.* **2018**, *121*, No. 167402.
(25) Pető, J.; et al. Spontaneous doping of the basal plane of MoS_2 single layers through oxygen substitution under ambient conditions. *Nat. Chem.* **2018**, *10*, 1246−1251.
(26) Amani, M.; et al. Near-unity photoluminescence quantum yield in MoS_2. *Science.* **2015**, *350*, 1065−1068.
(27) Vancso, P.; Magda, G. Z.; Peto, J.; Noh, J.-Y.; Kim, Y.-S.; Hwang, C.; Biro, L. P.; Tapaszto, L. The intrinsic defect structure of exfoliated MoS_2 single layers revealed by Scanning Tunneling Microscopy. *Sci. Rep.* **2016**, *6*, 1−7.
(28) Komsa, H. P.; Krasheninnikov, A. V. Native defects in bulk and monolayer MoS_2 from first principles. *Phys. Rev. B* **2015**, *91*, 1−17.
(29) Hong, J.; Hu, Z.; Probert, M.; Li, K.; Lv, D.; Yang, X.; Gu, L.; Mao, N.; Feng, Q.; Xie, L.; et al. Exploring atomic defects in molybdenum disulphide monolayers. *Nat. Commun.* **2015**, *6*, 1−8.
(30) Tumino, F.; Casari, C. S.; Li Bassi, A.; Tosoni, S. Nature of Point Defects in Single-Layer MoS_2 Supported on Au(111). *J. Phys. Chem. C* **2020**, *124*, 12424−12431.
(31) Ansh, A.; Patbhaje, U.; Kumar, J.; Meersha, A.; Shrivastava, M. Origin of electrically induced defects in monolayer MoS_2 grown by chemical vapor deposition. *Commun. Mater.* **2023**, *4*, 1−11.
(32) Van Der Zande, A. M.; et al. Grains and grain boundaries in highly crystalline monolayer molybdenum disulphide. *Nat. Mater.* **2013**, *12*, 554−561.
(33) Zhou, W.; et al. Intrinsic structural defects in monolayer molybdenum disulfide. *Nano Lett.* **2013**, *13*, 2615−2622.
(34) Najmaei, S.; et al. Vapour phase growth and grain boundary structure of molybdenum disulphide atomic layers. *Nat. Mater.* **2013**, *12*, 754−759.
(35) Mouri, S.; Miyauchi, Y.; Matsuda, K. Tunable photoluminescence of monolayer MoS_2 via chemical doping. *Nano Lett.* **2013**, *13*, 5944−5948.
(36) Peimyoo, N.; et al. Chemically driven tunable light emission of charged and neutral excitons in monolayer WS_2. *ACS Nano* **2014**, *8*, 11320−11329.
(37) Mak, K. F.; Shan, J. Photonics and optoelectronics of 2D semiconductor transition metal dichalcogenides. *Nat. Photonics.* **2016**, *10*, 216−226.
(38) Zhang, S.; Hill, H. M.; Moudgil, K.; Richter, C. A.; Hight Walker, A. R.; Barlow, S.; Marder, S. R.; Hacker, C. A.; Pookpanratana, S. J. Controllable, Wide-Ranging n-Doping and p-Doping of Monolayer Group 6 Transition-Metal Disulfides and Diselenides. *Adv. Mater.* **2018**, *30* (36), No. 1802991.
(39) Li, M.; et al. P-type Doping in Large-Area Monolayer MoS_2 by Chemical Vapor Deposition. *ACS Appl. Mater. Interfaces.* **2020**, *12*, 6276−6282.
(40) Chen, J.; et al. Photoluminescence modulation and charge transfer dynamics in R6G-decorated monolayer WS_2. *J. Lumin.* **2023**, *257*, No. 119695.
(41) Ross, J. S.; et al. Electrically tunable excitonic light-emitting diodes based on monolayer WSe_2 p − n junctions. *Nat. Nanotechnol.* **2014**, *9*, 268−272.
(42) Li, P.; Chaturvedi, A.; Zhou, H.; Zhang, G.; Li, Q.; Xue, J.; Zhou, Z.; Wang, S.; Zhou, K.; Weng, Y.; et al. Electrostatic Coupling in $MoS_2/CuInP_2S_6$ Ferroelectric vdW Heterostructures. *Adv. Funct. Mater.* **2022**, *32* (29), No. 2201359.
(43) Tanoh, A. O. A.; et al. Giant photoluminescence enhancement in $MoSe_2$ monolayers treated with oleic acid ligands. *Nanoscale Adv.* **2021**, *3*, 4216−4225.
(44) Li, Z.; Bretscher, H.; Zhang, Y.; Delport, G.; Xiao, J.; Lee, A.; Stranks, S. D.; Rao, A. Mechanistic insight into the chemical treatments of monolayer transition metal disulfides for photoluminescence enhancement. *Nat. Commun.* **2021**, *12*, 6044.
(45) Kim, H.; Lien, D. H.; Amani, M.; Ager, J. W.; Javey, A. Highly Stable Near-Unity Photoluminescence Yield in Monolayer MoS_2 by

https://doi.org/10.1021/acsnano.5c08927
ACS Nano 2025, 19, 34698−34707

Fluoropolymer Encapsulation and Superacid Treatment. *ACS Nano* **2017**, *11*, 5179−5185.
(46) Li, Z.; et al. Synchronized Photoluminescence and Electrical Mobility Enhancement in 2D WS_2 through Sequence-Specific Chemical Passivation. *J. Am. Chem. Soc.* **2024**, *146* (51), 35146−35154.
(47) Zhang, M.; et al. Super-resolved Optical Mapping of Reactive Sulfur-Vacancies in Two-Dimensional Transition Metal Dichalcogenides. *ACS Nano* **2021**, *15*, 7168−7178.
(48) Schwarz, A.; Alon-Yehezkel, H.; Levi, A.; Yadav, R. K.; Majhi, K.; Tzuriel, Y.; Hoang, L.; Bailey, C. S.; Brumme, T.; Mannix, A. J.; et al. Thiol-based defect healing of WSe_2 and WS_2. *npj 2D Mater. Appl.* **2023**, *7*, 1−9.
(49) Bretscher, H.; et al. Rational Passivation of Sulfur Vacancy Defects in Two-Dimensional Transition Metal Dichalcogenides. *ACS Nano* **2021**, *15*, 8780−8789.
(50) Zhang, X.; et al. Influence of Carbon in Metalorganic Chemical Vapor Deposition of Few-Layer WSe_2 Thin Films. *J. Electron. Mater.* **2016**, *45*, 6273−6279.
(51) Choudhury, T. H.; et al. Chalcogen Precursor Effect on Cold-Wall Gas-Source Chemical Vapor Deposition Growth of WS_2. *Cryst. Growth Des.* **2018**, *18*, 4357−4364.
(52) Jiao, T.; Leu, G. L.; Farrell, G. J.; Burkey, T. J. Photoacoustic calorimetry and quantum yields of $Mo(CO)_6$ ligand exchange in linear alkanes: Determination of volume of reaction, energetics, and kinetics of nucleophile displacement of alkane from $Mo(CO)_5$(alkane). *J. Am. Chem. Soc.* **2001**, *123*, 4960−4965.
(53) Shi, L. Challenges remain for 2D semiconductor growth. *Nat. Nanotechnol.* **2024**, *19*, 145.
(54) Kang, K.; et al. High-mobility three-atom-thick semiconducting films with wafer-scale homogeneity. *Nature* **2015**, *520*, 656−660.
(55) Yu, M.; et al. Polymorphism of Segmented Grain Boundaries in Two-Dimensional Transition Metal Dichalcogenides. *Nano Lett.* **2021**, *21*, 6014−6021.
(56) Ataca, C.; Şahin, H.; Ciraci, S. Stable, single-layer MX_2 transition-metal oxides and dichalcogenides in a honeycomb-like structure. *J. Phys. Chem. C* **2012**, *116*, 8983−8999.
(57) Bussolotti, F.; Goh, K. E. J.; Yang, J.; Kawai, H.; Wong, C. P. Y. Impact of s-vacancies on the charge injection barrier at the electrical contact with the MoS_2 monolayer. *ACS Nano* **2021**, *15*, 2686−2697.
(58) Zhang, X.; et al. Promoting the conversion of Li_2S by functional additives phenyl diselenide in Lithium−Sulfur batteries. *J. Power Sources* **2021**, *482* (15), No. 228967.
(59) Mak, K. F.; et al. Tightly bound trions in monolayer MoS_2. *Nat. Mater.* **2013**, *12*, 207−211.
(60) Michail, A.; Delikoukos, N.; Parthenios, J.; Galiotis, C.; Papagelis, K. Optical detection of strain and doping inhomogeneities in single layer MoS_2. *Appl. Phys. Lett.* **2016**, *108*, 173102.
(61) Gorbachev, R. V.; et al. Hunting for monolayer boron nitride: Optical and raman signatures. *Small* **2011**, *7*, 465−468.
(62) Jang, J.; Kim, J.-K.; Shin, J.; Kim, J.; Baek, K.-Y.; Park, J.; Park, S.; Kim, Y. D.; Parkin, S. S. P.; Kang, K.; et al. Reduced dopant-induced scattering in remote charge-transfer-doped MoS_2 field-effect transistors. *Sci. Adv.* **2022**, *8*, 1−11.
(63) Tanoh, A. O. A.; et al. Enhancing Photoluminescence and Mobilities in WS_2 Monolayers with Oleic Acid Ligands. *Nano Lett.* **2019**, *19*, 6299−6307.
(64) Su, L.; Yu, Y.; Cao, L.; Zhang, Y. Correlative spectroscopic investigations of the mechanisms of inhomogeneity in CVD-grown monolayer WS_2. *Sci. China Mater.* **2023**, *66*, 3949−3957.
(65) Mouloua, D.; et al. Fabrication control of MoS_2/MoO_2 nanocomposite via chemical vapor deposition for optoelectronic applications. *Mater. Sci. Eng. B* **2022**, *286*, No. 116035.
(66) Kondekar, N. P.; Boebinger, M. G.; Woods, E. V.; McDowell, M. T. In Situ XPS Investigation of Transformations at Crystallographically Oriented MoS_2 Interfaces. *ACS Appl. Mater. Interfaces* **2017**, *9*, 32394−3240.
(67) Ganta, D.; Sinha, S.; Haasch, R. T. 2-D Material Molybdenum Disulfide Analyzed by XPS. *Surf. Sci. Spectra* **2014**, *21*, 19−27.
(68) Shutthanandan, V.; et al. Applications of XPS in the characterization of Battery materials. *J. Electron Spectrosc. Relat. Phenom.* **2019**, *231*, 2−10.
(69) Wang, X.; et al. Dense-Stacking Porous Conjugated Polymer as Reactive-Type Host for High-Performance Lithium Sulfur Batteries. *Angew. Chem.* **2021**, *60*, 11359−11369.
(70) Hareendrakrishnakumar, H.; Chulliyote, R.; Joseph, M. G. Ion-selective PEDOT:PSS-decorated separator as a potential polysulfide immobilizer for lithium-sulfur batteries. *Ionics.* **2021**, *27*, 1087−1099.
(71) Li, Z.; Bretscher, H.; Rao, A. Chemical passivation of 2D transition metal dichalcogenides: strategies, mechanisms, and prospects for optoelectronic applications. *Nanoscale* **2024**, *16*, 9728−9741.
(72) Dong, Y.; Huang, C.; Yang, X. Y. Underwater superoleophobic and underoil superhydrophobic surface made by liquid-exfoliated MoS_2 for on-demand oil-water separation. *Chem. Eng. J.* **2019**, *361*, 322−328.
(73) Jeong, W.; Kim, T.; Kim, Y.; Jeong, M. S.; Kim, E. K. Improved characteristics of MoS_2 transistors with selective doping using 1,2-dichloroethane. *Semicond. Sci. Technol.* **2023**, *38*, 075013.
(74) Frisch, M. J. et al. *Gaussian 16*; Gaussian, Inc.: Wallingford, CT, 2016.
(75) Kresse, G.; Furthmuller, J. Efficient iterative schemes for ab initio total-energy calculations using a plane-wave basis set. *Phys. Rev. B* **1996**, *54*, 11169.
(76) Perdew, J. P.; Burke, K.; Ernzerhof, M. Generalized Gradient Approximation Made Simple. *Phys. Rev. B* **1996**, *77*, 3865.
(77) Grimme, S.; Ehrlich, S.; Goerigk, L. Effect of the damping function in dispersion corrected density functional theory. *J. Comput. Chem.* **2011**, *32*, 1456−1465.
(78) Krukau, A. V.; Vydrov, O. A.; Izmaylov, A. F.; Scuseria, G. E. Influence of the exchange screening parameter on the performance of screened hybrid functionals. *J. Chem. Phys.* **2006**, *125*, No. 224106.

https://doi.org/10.1021/acsnano.5c08927
ACS Nano 2025, 19, 34698−34707